Hindawi
International Journal of Intelligent Systems
Volume 2023, Article ID 8813500, 16 pages
https://doi.org/10.1155/2023/8813500

WILEY | Hindawi

Research Article

Nonconvex Regularization with Multi-Weighted Strategy for Real Color Image Denoising

Ying Shi,[1] Tianyu Liu,[2] Dong Hu,[2] Chuan Li,[3] and Zhi Wang[2]

[1]*Information Construction Office, Southwest University, Chongqing 400715, China*
[2]*College of Computer and Information Science, Southwest University, Chongqing 400715, China*
[3]*Big Data and Intelligence Engineering School, Chongqing College of International Business and Economics, Chongqing 401520, China*

Correspondence should be addressed to Zhi Wang; chiw@swu.edu.cn

Received 12 May 2023; Revised 23 August 2023; Accepted 10 September 2023; Published 25 September 2023

Academic Editor: Alexander Hošovský

Most existing image denoising methods commonly assume that the image is contaminated by additive white Gaussian noise (AWGN). However, real-world color image noise exhibits more complicated distribution properties, making it challenging to develop an accurate model. Consequently, denoising methods designed for AWGN often fail to achieve satisfactory performance on real-world images. In this paper, we present a novel multi-channel optimization model for real-world color images denoising within the multi-weighted Schatten p-norm minimization. Our proposed model utilizes the weighted Schatten p-norm as the regularization term, while the data fidelity term employs two weight matrices to balance the noise level across channels and regions. Besides, it helps to preserve as much detail as possible in the recovered image while removing noise. Although our proposed model is nonconvex and has no analytical solution, an accurate and efficient optimization algorithm is established based on the alternating direction method of multipliers (ADMMs) framework. Finally, we demonstrate the superior performance of our proposed method over existing state-of-the-art models on three real image datasets.

1. Introduction

During the process of image acquisition and dissemination, the quality of the acquired images is influenced by a plethora of factors, including environmental conditions and equipment characteristics [1]. These can give rise to noise artifacts that hinder the effective extraction of information from the imagery, ultimately limiting its utility in subsequent processing tasks, such as image classification [2, 3], segmentation [4, 5], and recognition [6, 7]. In general, image denoising is to recover a clean image $\mathbf{x}$ from a noisy image $\mathbf{y} = \mathbf{x} + \mathbf{n}$, where $\mathbf{n}$ is usually assumed to be the additive white Gaussian noise (AWGN), endowed with a constant distribution intensity [8–13]. However, AWGN is an idealized model that assumes a specific probability distribution and intensity for noise, which may not accurately reflect real-world situations. In practice, realistic noise has a complex distribution that is signal independent and influenced by various parameters of the capture device [14]. Therefore, real image denoising is a challenging task that requires more attention.

In the past two decades, various methods have been proposed for denoising images, which can be broadly classified into the following categories: filtering-based [11, 15], sparse coding-based [7, 16–18], low-rank-based [12, 19–22], deep learning-based [13, 23–27], and hybrid methods [28, 29]. The majority of existing methods are intended to remove AWGN or reduce noise in grayscale images. Unfortunately, Xu et al. [20] demonstrated that applying gray image denoising directly to color images does not yield satisfactory results. This is because the noise levels between image channels tend to differ. In the last 10 years, deep learning approaches have shown promising results in denoising color images affected by AWGN. However, these methods are highly dependent on the training dataset and often fail to generalize well to real-world images. As a result,

there is a need to develop a more robust denoising method based on a more accurate model that can effectively tackle the challenges posed by real-world color image denoising.

Recently, the low-rank minimization model [30–34] has received considerable attention due to its superior performance in image denoising. Since image is considered to have low-rank property, numerous methods have been proposed based on this property. However, in the realm of low-rank minimization models, the widely employed convex nuclear norm minimization leads to overshrinking of large singular values containing more dominant information, thus yielding biased solutions. To counter this limitation, researchers have delved into nonconvex optimization techniques, aiming to more precisely capture the inherent low-rank characteristics of the image. For instance, Gu et al. proposed the weighted nuclear norm minimization (WNNM) model [12] and applied it to image denoising. It ensures information preservation by weighting the singular values so that larger one will be less penalized. However, WNNM still tends to overshrink the rank component, resulting in bad performance when noise level is high. To overcome this limitation, WSNM employs weighted Schatten p-norm instead of weighted nuclear norm, which provides a better approximation of the rank function. By setting the power parameter p appropriately, WSNM [35] offers greater flexibility and exhibits superior image denoising performance compared to WNNM. Unfortunately, WNNM and WSNM are initially developed for grayscale image denoising. Considering that noise level in the R, G, and B channels of color images, Xu et al. [20] proposed the MCWNNM, which extends WNNM to perform color image denoising. To address the same issues encountered with WNNM, Huang et al. [21] proposed the MCWSNM and achieved excellent results on real-world color image denoising. Shan et al. [36] introduced a novel multi-channel optimization framework for color image denoising, utilizing nuclear norm minus Frobenius norm minimization. Furthermore, Chen et al. [37] innovatively represented color images as pure quaternion matrices and then applied low-rank constraints to these constructed quaternion matrices, effectively harnessing the inherent cross-channel correlation within color channels.

Real-world images captured by CCD or CMOS cameras exhibit complex characteristics. These characteristics may be signal dependent, which can vary with different camera settings (such as ISO, shutter speed, and aperture). While MCWNNM and MCWSNM have shown promising results in real-world image denoising, both of them do not consider the variation in noise level across patches in the real-world image. To address the above issues, we introduce a new weight matrix to balance the noise differences across various patches and propose a novel image denoising model based on multi-weighted Schatten p-norm minimization. Our proposed model has three main merits. First, we use the weighted Schatten p-norm as the rank surrogate to accurately approximate the rank function, which helps to preserve as much detail as possible in the recovered image while removing noise. Second, we incorporate two weight matrices in our proposed model to balance the noise between different channels and patches. This makes our model more realistic and the recovered images closer to clean images. Third, we utilize the alternating direction method of multipliers (ADMMs) framework to decompose the nonconvex problem into several subproblems that can be easily calculated. This ensures the effectiveness and efficiency of our proposed method. Besides, we make a detailed analysis of the proposed algorithm, including complexity analysis, convergence analysis, and its theoretical proof. Finally, extensive experiments are conducted to demonstrate the superior performance of our proposed method in real-world color image denoising compared to existing state-of-the-art models.

This paper is structured as follows. In Section 2, we present the related work, including the application of low-rank matrix approximation methods to image denoising and real-world image denoising. Section 3 presents the proposed multi-weighted Schatten p-norm minimization model, the optimization method, and the theoretical analysis of the proposed algorithm. In Section 4, the denoising performance of our proposed method is compared with some state-of-the-art methods on three real image datasets. Finally, we summarize our work in Section 5.

2. Related Work

In this section, we first introduce the methods of low-rank matrix approximation in image denoising and then discuss the approaches for real-world image denoising.

2.1. Existing Rank Minimization Methods for Color Image Denoising. The color image denoising model based on low-rank minimization relies on the assumption that natural color images exhibit nonlocal similarity (NSS) [38]. In [19], Dong et al. demonstrated that low-rank minimization can be effectively utilized in image denoising by establishing NSS. NSS suggests that a given pixel or patch of an image can be well represented by similar pixels or patches located elsewhere in the image, rather than just those adjacent neighbors. Therefore, by exploiting NSS, a latent clean matrix can be obtained by performing a low-rank minimization procedure on each patch-generated matrix and then it can be merged to create a noise-free image.

Among the low-rank minimization models, nuclear norm minimization (NNM) [39, 40] is the most commonly used method. However, it treats all singular values equally, which can lead to overshrinking of large singular values that contain more dominant information. To address this issue, Gu et al. proposed the weighted nuclear norm minimization (WNNM) model [12], which can be formulated as

$$\min_{\mathbf{x}} \frac{1}{\sigma^2}\|\mathbf{Y}-\mathbf{X}\|_F^2 + \|\mathbf{X}\|_{\mathbf{w},*}, \tag{1}$$

where $\mathbf{X}$ and $\mathbf{Y}$ denote the matrix composed of similar patches in the latent clean image and noisy image, respectively. $\|\mathbf{X}\|_{\mathbf{w},*} = \sum_{i=1}^{r} w_i \sigma_i(\mathbf{X})$ is the weighted nuclear norm of matrix $\mathbf{X}$, $\mathbf{w} = [w_1, w_2, \ldots, w_n]^\top$ is the nondescending weight vector with $0 \le w_1 \le w_2 \le \ldots \le w_n$, and $\sigma_i(\mathbf{X})$ is the i-th singular value of $\mathbf{X}$. $\|\mathbf{X}\|_F = \sqrt{\mathrm{tr}(\mathbf{X}^\top\mathbf{X})}$ is the

Frobenius norm of $\mathbf{X}$. σ is the standard deviation of added AWGN noise.

Although WNNM has been shown to achieve good denoising results, several improved models have been proposed [20, 35, 36, 41, 42]. In [20], Xu et al. proposed the MCWNNM, extending WNNM to perform color image denoising, which can be formulated as

$$\min_{\mathbf{x}} \|\mathbf{W}(\mathbf{Y}-\mathbf{X})\|_F^2 + \|\mathbf{X}\|_{\mathbf{w},*}, \tag{2}$$

with $\mathbf{W} = (\sigma_r^{-1}\mathbf{I}, \sigma_g^{-1}\mathbf{I}, \sigma_b^{-1}\mathbf{I})$. $\mathbf{W}$ is the weight matrix characterizing the noise levels in different channels. $\mathbf{I}$ is the unit matrix. $\sigma_r, \sigma_g, \sigma_b$ are the standard deviations of noise in R, G, and B channels, respectively. In [21], Huang et al. proposed the MCWSNM with the same weighted strategy, which can be formulated as

$$\min_{\mathbf{x}} \|\mathbf{W}(\mathbf{Y}-\mathbf{X})\|_F^2 + \|\mathbf{X}\|_{\mathbf{w},Sp}^p, \tag{3}$$

where weighted Schatten p-norm $\|\mathbf{X}\|_{\mathbf{w},Sp}^p = (\sum_{i=1}^r w_i \sigma_i^p)^{1/p}$ and power $p \in (0, 1]$.

Currently, MCWSNM is considered a highly competitive method for color image denoising. Building upon the MCWSNM, we introduce a new weight matrix to balance the noise differences across various patches and propose a novel model for real-world color image denoising.

2.2. Real-World Image Denoising. Over the last few decades, researchers have extensively studied the denoising of AWGN. However, it is essential to acknowledge that AWGN is an artificial addition that is used to simulate noise in real-world scenarios. It is assumed to follow a specific probability distribution, which may not necessarily reflect the actual characteristics of noise in the real world as it often remains unknown. As a result, real-world image denoising methods can be categorized into two groups based on whether or not they rely on the noise levels as input.

We first discuss methods that require the noise level as input. Since real-world noise is typically unknown, numerous methods have been proposed to estimate the noise level [43–45]. Denoising color images has been a challenging task, and several methods have been proposed to tackle this problem. For instance, color block-matching 3D (CBM3D) [46] first converts the sRGB image into the luminance-chromaticity space and applies BM3D separately to each channel. However, the color space conversion complicates the structure of the noise and does not fully leverage the correlation between the channels. LSSC [16] was the first method to suggest combining sparse coding with NSS for image denoising. To suppress sparse coding noise, Zhang et al. [18] introduced the concept of sparse coding noise and shifted the focus of image restoration. Nevertheless, the efficacy of sparse coding methods remains contingent upon the selection of a suitable dictionary, while the task of identifying the optimal dictionary to accurately represent a signal or image patch remains a formidable challenge. By utilizing the inherent low-rank characteristic of the NSS generating matrix, the low-rank model attains remarkable performance in image denoising. Considering that the noise level varies in each channel of a color image, MCWNNM [20], based on WNNM [12], introduces a weight matrix to balance the noise in different channels of color images. In addition, MCWSNM [21] introduces a weighted Schatten p-norm to tackle the issue of overshrinking singular values of the weighted nuclear norm and adds flexibility to the denoising process. However, these methods do not consider the patchwise variation of noise in the spatial domain.

We then discuss methods that do not require an input noise level, commonly referred to as blind denoising. For instance, Lebrun et al. [47] proposed a blind image algorithm that can operate on arbitrary digital images as input. This method estimates a signal and frequency-dependent (SFD) noise and subsequently denoises the image by employing a multi-scale adaptation of a nonlocal Bayesian denoising method. Xu et al. [48] employed a nonlocal self-similarity prior to denoise patch group- (PG-) based images, using nonparametric Bayesian dictionary learning to extract potentially clean structures from PG variations. In addition, a number of deep learning-based blind denoising methods have been proposed. Wang et al. [49] developed an end-to-end structured multi-column convolutional neural network (MC-Net) to train a denoiser using known noise levels, which was then utilized to estimate the noise levels. Guo et al. [26] combined synthetic noise data with real data to train the convolutional blind denoising network (CBDNet), resulting in improved generalization ability of model and enhanced denoising effectiveness. While deep learning has undoubtedly secured a dominant role in computer vision, it also comes with its own set of challenges compared with traditional methods. These include heavy dependence on datasets, leading to potential overfitting, and a lack of rigorous theoretical foundations.

Our approach introduces two weight matrices to model the distinct noise distribution across channels and spatial patches in real-world images, aiming to further improve the denoising performance of real-world color images. Moreover, we provide the theoretical underpinnings of our proposed method and conduct a convergence analysis for the proposed optimization algorithm.

3. Multi-Weighted Schatten p-Norm Minimization for Real-World Image Denoising

In this section, we first present the weighted Schatten p-norm minimization model for color image denoising and then establish an efficient algorithm to solve the proposed model by using the framework of ADMM.

3.1. Problem Formulation. The problem of real color image denoising aims to recover the clean image $\mathbf{x}_{\text{cm}}$ for its noisy observation $\mathbf{y}_{\text{cm}}$:

$$\mathbf{y}_{\text{cm}} = \mathbf{x}_{\text{cm}} + \mathbf{n}_{\text{cm}}, \tag{4}$$

where $c \in \{r, g, b\}$ is the index of R, G, and B channels in color image, $m \in \{1, 2, \ldots, M\}$ is the index of the patch number, and $\mathbf{n}_{\mathrm{cm}}$ refers to noise level in m-th patch of channel c.

In the past decade, low-rank minimization methods have demonstrated remarkable denoising performance by exploiting the low-rank property of redundant nonlocal similarity over an image. To denoise a noisy image $\mathbf{y}_{\mathrm{cm}}$, we identify a set of key patches sized $p \times p$ with a fixed interval across the image. For each key patch, we select M most similar patches, including itself, in a search window. The similarity between two patches is measured using the Euclidean distance. For each similar patch, we reshape it as a column vector $\mathbf{v}_{\mathrm{cm}} \in \mathbb{R}^{p^2}$, where $\mathbf{v} = \{\mathbf{y}, \mathbf{x}, \mathbf{n}\}$ denotes the noisy image, the clean image, and the noise, respectively. By arranging the M vectors in each channel, we can obtain a matrix $\mathbf{M}_{\mathbf{c}} = [\mathbf{v}_{c1}^{\top}, \mathbf{v}_{c2}^{\top}, \ldots, \mathbf{v}_{\mathrm{cM}}^{\top}]$, and $\mathbf{M} = [\mathbf{M}_r^{\top}, \mathbf{M}_g^{\top}, \mathbf{M}_b^{\top}]$ denotes the matrix combined by all channels. Then, we use $\mathbf{Y} = \mathbf{X} + \mathbf{N}$ to represent a matrix stacking by M similar patches in the noisy image, where $\mathbf{Y}$ denotes the noisy image, $\mathbf{X}$ is the latent clean image, and $\mathbf{N}$ is the noise values. The entire clean image can then be generated by all denoised patches.

The distribution of noise in real-world images varies not only in each color channel but also in each patch. To address this issue effectively, we propose a multi-weighted Schatten p-norm minimization model for denoising real-world color images. The proposed model is defined as follows:

$$\min_{\mathbf{X}} \left\| \mathbf{W}_1 (\mathbf{Y} - \mathbf{X}) \mathbf{W}_2 \right\|_F^2 + \|\mathbf{X}\|_{\mathbf{w}, S_p}^p, \tag{5}$$

where $\mathbf{W}_1$ represents the weight matrix employed to characterize the diverse noise levels in R, G, and B channels and $\mathbf{W}_2$ refers to the weight matrix for describing different noise levels between individual patches. The definition of $\mathbf{W}_1$ and $\mathbf{W}_2$ is discussed in the next subsection. According to the definition in [21], we set the weight of the weighted Schatten p-norm to be $w_i = c\sqrt{M}/(\sigma_i(\mathbf{X}) + \epsilon)$ based on empirical evidence. Here, $c > 0$ is a constant, and $\epsilon = 10^{-16}$ is a parameter that is used to prevent division by zero. M is the number of similar patches, and $\sigma_i(\mathbf{X})$ represents the i-th singular values of $\mathbf{X}$.

3.2. Definition of Weighted Matrices. The values of $\mathbf{W}_1$ and $\mathbf{W}_2$ are determined using the maximum a posteriori (MAP) estimation framework [50]. To obtain the MAP estimate of matrix $\mathbf{X}$, given the observation matrix $\mathbf{Y}$, we maximize the log posterior probability as follows:

$$\begin{aligned} \widehat{\mathbf{X}} &= \arg \max_{\mathbf{X}} \ln P(\mathbf{X} \mid \mathbf{Y}) \\ &= \arg \max_{\mathbf{X}} \{\ln P(\mathbf{Y} \mid \mathbf{X}) + \ln P(\mathbf{X})\}. \end{aligned} \tag{6}$$

Here, the likelihood term $P(\mathbf{X} \mid \mathbf{Y})$ is used to model the statistics of the noise. As posited by Leung et al. [50], it can be assumed that the noise is independently and identically (i.i.d.) distributed in every patch and channel, following a Gaussian distribution. Thus, we have $\mathbf{n}_c \sim \mathcal{N}(0, \sigma_c)$ and $\mathbf{n}_m \sim \mathcal{N}(0, \sigma_m)$, where $\mathbf{n}_c$ and $\mathbf{n}_m$ denote the noise levels in channel c and the m-th patch, respectively. According to the log-linear model, the relationship between σ_c and σ_m can be modeled as $\sigma_{cm} = \sigma_c^{\ell_1} \sigma_m^{\ell_2}$ where $\ell_1 + \ell_2 = 1$. Empirically, we consider σ_c and σ_m are of equal significance, so we set $\sigma_c = \sigma_m = 1/2$ and define the noise of m-th patch in channel c as $\mathbf{n}_{\mathrm{cm}} = \mathbf{y}_{\mathrm{cm}} - \mathbf{x}_{\mathrm{cm}} \sim \mathcal{N}(0, \sigma_{\mathrm{cm}})$. Therefore, $P(\mathbf{X} \mid \mathbf{Y})$ can be formulated as

$$P(\mathbf{Y} \mid \mathbf{X}) = \prod_{c \in \{r,g,b\}} \prod_{m=1}^{M} \left(\sqrt{2\pi}\, \sigma_{\mathrm{cm}}\right)^{-3q^2 M} \exp\left(-\frac{\left\| \mathbf{y}_{\mathrm{cm}} - \mathbf{x}_{\mathrm{cm}} \right\|_2^2}{2\sigma_{\mathrm{cm}}^2} \right). \tag{7}$$

Since the minimum Schatten p-norm property is imposed on underlying latent clean image $\mathbf{X}$, we let $P(\mathbf{X})$ be

$$P(\mathbf{X}) \propto \exp\left(-\frac{1}{2} \|\mathbf{X}\|_{\mathbf{w}, \mathrm{Sp}}^p \right). \tag{8}$$

Putting (7) and (8) into (6), we obtain

$$\begin{aligned} \widehat{\mathbf{X}} &= \arg\min_{\mathbf{X}} \sum_{c \in \{r,g,b\}} \sum_{m=1}^{M} \frac{1}{\sigma_{\mathrm{cm}}^2} \left\| \mathbf{y}_{\mathrm{cm}} - \mathbf{x}_{\mathrm{cm}} \right\|_2^2 + \|\mathbf{X}\|_{\mathbf{w}, \mathrm{Sp}}^p \\ &= \arg\min_{\mathbf{X}} \sum_{c \in \{r,g,b\}} \frac{1}{\sigma_c} \left\| (\mathbf{Y}_c - \mathbf{X}_c) \mathbf{W}_2 \right\|_F^2 + \|\mathbf{X}\|_{\mathbf{w}, \mathrm{Sp}}^p \\ &= \arg\min_{\mathbf{X}} \left\| \mathbf{W}_1 (\mathbf{Y} - \mathbf{X}) \mathbf{W}_2 \right\|_F^2 + \|\mathbf{X}\|_{\mathbf{w}, \mathrm{Sp}}^p, \end{aligned} \tag{9}$$

with $\mathbf{W}_1 = \begin{pmatrix} \tau_r^{-1/2} \mathbf{I}_{p^2} & 0 & 0 \\ 0 & \tau_g^{-1/2} \mathbf{I}_{p^2} & 0 \\ 0 & 0 & \tau_b^{-1/2} \mathbf{I}_{p^2} \end{pmatrix}$, $\mathbf{W}_2 = \begin{pmatrix} \sigma_1^{-1/2} & 0 & 0 \\ 0 & \ddots & 0 \\ 0 & 0 & \sigma_M^{-1/2} \end{pmatrix}$, where $(\tau_r, \tau_g, \tau_b) = \min\{\sigma_r, \sigma_g, \sigma_b\} / (\sigma_r, \sigma_g, \sigma_b)$.

3.3. Optimization Algorithm. There is no analytical solution to the proposed model (5) due to its nonconvex property. Fortunately, we can utilize the alternating direction method of multipliers (ADMMs) framework to decompose the problem into a set of subproblems that can be solved iteratively. To achieve this, we introduce an auxiliary variable $\mathbf{Z}$, which allows us to rewrite model (5) as follows:

$$\begin{aligned} &\min_{\mathbf{X}, \mathbf{Z}} \left\| \mathbf{W}_1 (\mathbf{Y} - \mathbf{X}) \mathbf{W}_2 \right\|_F^2 + \|\mathbf{Z}\|_{\mathbf{w}, \mathrm{Sp}}^p \\ &\text{s.t. } \mathbf{X} = \mathbf{Z}. \end{aligned} \tag{10}$$

The augmented Lagrangian function of (10) can be formulated as

$$\mathscr{L}(\mathbf{X},\mathbf{Z},\Lambda,\rho)=\left\|\mathbf{W_1}(\mathbf{Y}-\mathbf{X})\mathbf{W_2}\right\|_F^2+\|\mathbf{Z}\|_{\mathbf{w},\mathrm{Sp}}^p+\mathbf{\Lambda}^T(\mathbf{X}-\mathbf{Z})+\frac{\rho}{2}\|\mathbf{X}-\mathbf{Z}\|_F^2, \tag{11}$$

where $\mathbf{\Lambda}$ is the augmented Lagrange multiplier and $\rho>0$ is the parameter for penalty. Then, the subproblem can be achieved by minimizing each variable in turn while fixing the other variables. Consequently, problem (10) can be solved via following steps.

$$\mathbf{X}_{k+1}=\underset{\mathbf{X}}{\operatorname{argmin}}\left\|\mathbf{W}_1(\mathbf{Y}-\mathbf{X})\mathbf{W}_2\right\|_F^2+\mathbf{\Lambda}^T(\mathbf{X}-\mathbf{Z}_k)+\frac{\rho_k}{2}\left\|\mathbf{X}-\mathbf{Z}_k\right\|_F^2, \tag{12}$$

$$\mathbf{Z}_{k+1}=\underset{\mathbf{Z}}{\operatorname{argmin}}\left\|\mathbf{Z}-\left(\mathbf{X}_{k+1}+\rho_k^{-1}\mathbf{\Lambda}_k\right)\right\|_F^2+\|\mathbf{Z}\|_{\mathbf{w},\mathrm{Sp}}^p, \tag{13}$$

$$\mathbf{\Lambda}_{k+1}=\mathbf{\Lambda}_k+\rho_k(\mathbf{X}_{k+1}-\mathbf{Z}_{k+1}), \tag{14}$$

$$\rho_{k+1}=\min\{\mu*\rho_k,\rho_{\max}\}. \tag{15}$$

(1) **Updating X**: to obtain $\mathbf{X}$, we derive it from the right part of (12), which yields the following equation:

$$\mathbf{W}_1^\top\mathbf{W}_1\mathbf{X}+\frac{\rho_k}{2}\mathbf{X}\left(\mathbf{W}_2\mathbf{W}_2^\top\right)^{-1}=\mathbf{W}_1^\top\mathbf{W}_1\mathbf{Y}_k+\left(\frac{\rho_k}{2}\mathbf{Z}_k-\frac{1}{2}\mathbf{\Lambda}_k\right)\left(\mathbf{W}_2\mathbf{W}_2^T\right)^{-1}. \tag{16}$$

Equation (16) is a standard Sylvester's equation which aims to find possible matrix $\mathbf{X}$ from given matrices $\mathbf{A},\mathbf{B}$, and $\mathbf{C}$ that satisfies the following equation:

$$\mathbf{AX}+\mathbf{XB}=\mathbf{C}. \tag{17}$$

Let

$$\begin{aligned}\mathbf{A}&=\mathbf{W}_1^\top\mathbf{W}_1,\\ \mathbf{B}&=\frac{\boldsymbol{\rho}_\mathbf{k}}{\mathbf{2}}\left(\mathbf{W}_2\mathbf{W}_2^\top\right)^{-1},\\ \mathbf{C}&=\mathbf{W}_1^\top\mathbf{W}_1\mathbf{Y}_\mathbf{k}+\left(\frac{\boldsymbol{\rho}_\mathbf{k}}{\mathbf{2}}\mathbf{Z}_\mathbf{k}-\frac{\mathbf{1}}{\mathbf{2}}\mathbf{\Lambda}_\mathbf{k}\right)\left(\mathbf{W}_2\mathbf{W}_2^\mathbf{T}\right)^{-1},\end{aligned} \tag{18}$$

in (17). By using Kronecker product $\otimes$ and the vectorization operator vec, we can rewrite Sylvester's equation in the form

$$\left(\mathbf{I}_M\otimes\mathbf{A}+\mathbf{B}^T\otimes\mathbf{I}_{3p^2}\right)\mathrm{vec}(\mathbf{X})=\mathrm{vec}(\mathbf{C}). \tag{19}$$

Then, we can get the solution of (12) as

$$\mathbf{X}_{k+1}=\mathrm{vec}^{-1}\left(\left(\mathbf{I}_M\otimes\mathbf{A}+\mathbf{B}^T\otimes\mathbf{I}_{3p^2}\right)^{-1}\mathrm{vec}(\mathbf{C})\right). \tag{20}$$

(2) **Updating Z**: (13) is a weighted Schatten p-norm minimization problem. Previous research [21] has shown that if the weights $\{w_i\}$ adhere to a non-descending permutation, then the optimization problem can be transformed into independent nonconvex subproblems of the l_p-norm. These subproblems can be solved efficiently using the generalized soft-thresholding (GST) algorithm. This procedure is summarized as Algorithm 1.

(3) **Updating Λ**: In the ADMM framework, the role of $\mathbf{\Lambda}$ is pivotal in managing constraints. It orchestrates updates, gradually aligning them with the optimization problem's constraints, thereby facilitating the algorithm in approximating the ultimate solution. $\mathbf{\Lambda}$ is updated as follows:

$$\mathbf{\Lambda}_{k+1}=\mathbf{\Lambda}_k+\rho_k(\mathbf{X}_{k+1}-\mathbf{Z}_{k+1}). \tag{21}$$

Here, ρ_k is a positive constant, often termed as the step size or penalty parameter, while $\mathbf{X}_{k+1}$ and $\mathbf{Z}_{k+1}$ correspond to the variables computed at iteration step $k+1$. The essence of this formulation lies in updating the Lagrange multiplier $\mathbf{\Lambda}$ progressively to better align with the constraints of the optimization problem. By adapting ρ_k and accounting for variations in the current variable $\mathbf{X}_{k+1}$, this iterative update gradually refines the Lagrange multiplier, thereby inching closer to the optimal solution.

(4) **Updating ρ**: The update parameter ρ in the ADMM algorithm is to regulate the convergence rate of the Lagrange multipliers. Mathematically, the update of ρ follows this formula:

$$\rho_{k+1} = \min\{\mu * \rho_k, \rho_{\max}\}. \tag{22}$$

Here, $\mu \geq 0$ is a step-size parameter, ρ_k corresponds to the parameter at the current iteration step, and $\rho_{\max}$ represents a predetermined upper threshold. This formula dynamically adjusts the parameter ρ used to penalize the constraints. By judiciously adapting this parameter, the algorithm strives for a more efficient approximation of the problem's solution.

Based on the above analysis, we summarize the optimization procedure for solving the proposed multi-weighted Schatten p-norm minimization model in Algorithm 2, and the flowchart of our proposed algorithm is shown in Figure 1.

3.4. Algorithm Analysis. We first discuss the computational complexity of our proposed algorithm. The computational cost of a single iteration in Algorithm 2 comprises two primary parts. The first part is updating $\mathbf{X}$. The primary computation here involves computing specific functions in Sylvester's equation, which incurs a cost of $O(\max\{M^3, (3p^2)^3\})$. The second component involves updating $\mathbf{Z}$. The primary cost here arises from the SVD operation in Algorithm 1, which costs $O(\max\{p^4M, p^2M^2\} + p^2r^4M)$. Given the parameter settings, we consider M to be significantly larger than p and r. Thus, the overall computational complexity of our proposed algorithm is $O(K_1M^3)$.

We then present a theorem that provides theoretical guarantee for the convergence of Algorithm 2.

Theorem 1. *Suppose the weight vector* $\mathbf{w}_i$ *is sorted in a nondescending order and the parameter* ρ_k *is unbounded. Under these conditions, the sequences* $\mathbf{X}_k$, $\mathbf{Z}_k$, *and* $\mathbf{\Lambda}_k$ *generated by Algorithm 2 satisfy the following:*

(a) $\lim_{k\longrightarrow\infty} \|\mathbf{X}_{k+1} - \mathbf{Z}_{k+1}\|_F = 0.$
(b) $\lim_{k\longrightarrow\infty} \|\mathbf{Z}_{k+1} - \mathbf{Z}_k\|_F = 0.$
(c) $\lim_{k\longrightarrow\infty} \|\mathbf{X}_{k+1} - \mathbf{X}_k\|_F = 0.$

Proof

(1) We first prove that the sequence of the augmented Lagrangian multiplier $\{\mathbf{\Lambda}_k\}$ is upper bounded. We let $\mathbf{U}_k[\mathrm{diag}(\sigma_1, \sigma_2, \ldots, \sigma_n)]\mathbf{V}_k^\top$ be the SVD of $(\rho_k^{-1}\mathbf{\Lambda}_k + \mathbf{X}_{k+1})$, and $\mathbf{Z}_k = \mathbf{U}_k[\mathrm{diag}(\delta_1, \delta_2, \ldots, \delta_n)]\mathbf{V}_k^\top$. Then we have:

$$\begin{aligned}
\left\|\|\mathbf{\Lambda}_{k+1}\|_F^2\right\| &= \left\|\mathbf{\Lambda}_k + \rho_k(\mathbf{X}_{k+1} - \mathbf{Z}_{k+1})\right\|_F^2 \\
&= \rho_k^2\left\|\rho_k^{-1}\mathbf{\Lambda}_k + \mathbf{X}_{k+1} - \mathbf{Z}_{k+1}\right\|_F^2 \\
&= \rho_k^2\left\|\mathbf{U}_k[\mathrm{diag}(\sigma_1, \sigma_2, \ldots, \sigma_n)]\mathbf{V}_k^\top - \mathbf{U}_k[\mathrm{diag}(\delta_1, \delta_2, \ldots, \delta_n)]\mathbf{V}_k^\top\right\|_F^2 \\
&= \rho_k^2\sum_{i=1}^{n}(\sigma_i - \delta_i)^2 \leq \rho_k^2\left\|\sum_{\mathbf{i=1}}^{\mathbf{n}}\frac{\mathbf{Jw_i}}{\boldsymbol{\rho}_\mathbf{k}}\right\|_2^2 = J^2\left\|\sum_{\mathbf{i=1}}^{\mathbf{n}}\mathbf{w_i}\right\|_2^2,
\end{aligned} \tag{23}$$

where J is the number of iterations in the GST algorithm. Thus, $\{\mathbf{\Lambda}_k\}$ is bounded.

(2) We then prove the sequence of the Lagrange function $\mathscr{L}_{k+1}(\mathbf{X}_{k+1}, \mathbf{Z}_{k+1}, \mathbf{\Lambda}_{k+1}, \rho_{k+1})$ is upper bounded.

$$\begin{aligned}
&\mathscr{L}(\mathbf{X}_{k+1}, \mathbf{Z}_{k+1}, \mathbf{\Lambda}_{k+1}, \rho_{k+1}) \\
&= \left\|\mathbf{W_1}(\mathbf{Y} - \mathbf{X_{k+1}})\mathbf{W_2}\right\|_F^2 + \left\|\mathbf{Z_{k+1}}\right\|_{\mathbf{w},S_p}^p \\
&\quad + \langle\mathbf{\Lambda}_{k+1}, \mathbf{X}_{k+1} - \mathbf{Z}_{k+1}\rangle + \frac{\rho_{k+1}}{2}\left\|\mathbf{X_{k+1}} - \mathbf{Z_{k+1}}\right\|_F^2 \\
&= \mathscr{L}(\mathbf{X}_{k+1}, \mathbf{Z}_{k+1}, \mathbf{\Lambda}_k, \rho_k)
\end{aligned}$$

Input: Noisy matrix $\mathbf{Y}$, weight vector $\{w_i\}_{i=1}^{r}$, p, iteration threshold K_2;
Initialize: $\mathbf{Y} = \mathbf{U}\Sigma\mathbf{V}^{\top}, \Sigma = \sigma_1, \sigma_2, \ldots, \sigma_r$;
(1) **for** $i = 1$: r **do**
(2) $\tau^{\mathrm{GST}}(\omega_i) = (2\omega_i(1-p))^{1/2-p} + \omega_i p(2\omega_i(1-p))^{p-1/2-p}$;
(3) **if** $|\sigma_i| \le \tau^{\mathrm{GST}}$ **then**
(4) $\delta_i = 0$;
(5) **else**
(6) $\delta_i^k = |\sigma_i|$;
(7) **for** $k = 1$: J **do**
(8) $\delta^{k+1} = |\sigma_i| - \omega_i p(\delta_i^k)^{p-1}$;
(9) $k \longleftarrow k+1$;
(10) **end for**
(11) $\delta_i = \mathrm{sgn}(\sigma_i)\delta_i^k$;
(12) **end if**
(13) $\Delta = \mathrm{diag}(\delta_1, \delta_2, \ldots, \delta_r)$;
(14) **end for**
(15) **Output** $\mathbf{Z}^* = \mathbf{U}\Delta\mathbf{V}^{\top}$.

Algorithm 1: Solving subproblem (13) by GST.

$$\begin{aligned}
&+\langle \Lambda_{k+1} - \Lambda_k, \mathbf{X}_{k+1} - \mathbf{Z}_{k+1}\rangle + \frac{\rho_{k+1}-\rho_k}{2}\left\|\mathbf{X}_{\mathbf{k+1}} - \mathbf{Z}_{\mathbf{k+1}}\right\|_F^2 \\
&= \mathscr{L}\left(\mathbf{X}_{k+1}, \mathbf{Z}_{k+1}, \Lambda_k, \rho_k\right) \\
&\quad + \langle \Lambda_{k+1} - \Lambda_k, \frac{\Lambda_{k+1} - \Lambda_k}{\rho_k}\rangle + \frac{\rho_{k+1}-\rho_k}{2}\left\|\frac{\Lambda_{\mathbf{k+1}} - \Lambda_{\mathbf{k}}}{\boldsymbol{\rho}_{\mathbf{k}}}\right\|_F^2 \\
&= \mathscr{L}\left(\mathbf{X}_{k+1}, \mathbf{Z}_{k+1}, \Lambda_k, \rho_k\right) + \frac{\rho_{k+1}+\rho_k}{2\rho_k^2}\left\|\Lambda_{\mathbf{k+1}} - \Lambda_{\mathbf{k}}\right\|_F^2.
\end{aligned} \tag{24}$$

Since Λ_k is upper bounded, the sequence $\{\Lambda_{k+1} - \Lambda_k\}$ is also upper bounded. Let u be the upper bound of $\{\Lambda_{k+1} - \Lambda_k\}$, i.e., $\forall k \ge 0, \|\Lambda_{k+1} - \Lambda_k\|_F \le u$, and we can obtain

$$\begin{aligned}
\mathscr{L}\left(\mathbf{X}_{k+1}, \mathbf{Z}_{k+1}, \Lambda_{k+1}, \rho_{k+1}\right) &\le \mathscr{L}\left(\mathbf{X}_{k+1}, \mathbf{Z}_{k+1}, \Lambda_k, \rho_k\right) + u^2\frac{\rho_{k+1}+\rho_k}{2\rho_k^2} \\
&\le \mathscr{L}\left(\mathbf{X}_1, \mathbf{Z}_1, \Lambda_0, \rho_0\right) + u^2\sum_{k=0}^{\infty}\frac{\rho_{k+1}+\rho_k}{2\rho_k^2} \\
&= \mathscr{L}\left(\mathbf{X}_1, \mathbf{Z}_1, \Lambda_0, \rho_0\right) + u^2\sum_{k=0}^{\infty}\frac{1+\mu}{2\rho_0\mu^k} \\
&\le \mathscr{L}\left(\mathbf{X}_1, \mathbf{Z}_1, \Lambda_0, \rho_0\right) + \frac{u^2}{\rho_0}\sum_{k=0}^{\infty}\frac{1}{\mu^{k-1}}.
\end{aligned} \tag{25}$$

Since $\sum_{k=0}^{\infty} 1/\mu^{k-1} < +\infty$, then we establish that $\mathscr{L}_{k+1}(\mathbf{X}_{k+1}, \mathbf{Z}_{k+1}, \Lambda_{k+1}, \rho_{k+1})$ is upper bonded.

(3) We next prove that the sequences of $\mathbf{X}_k$ and $\mathbf{Z}_k$ are upper bounded.

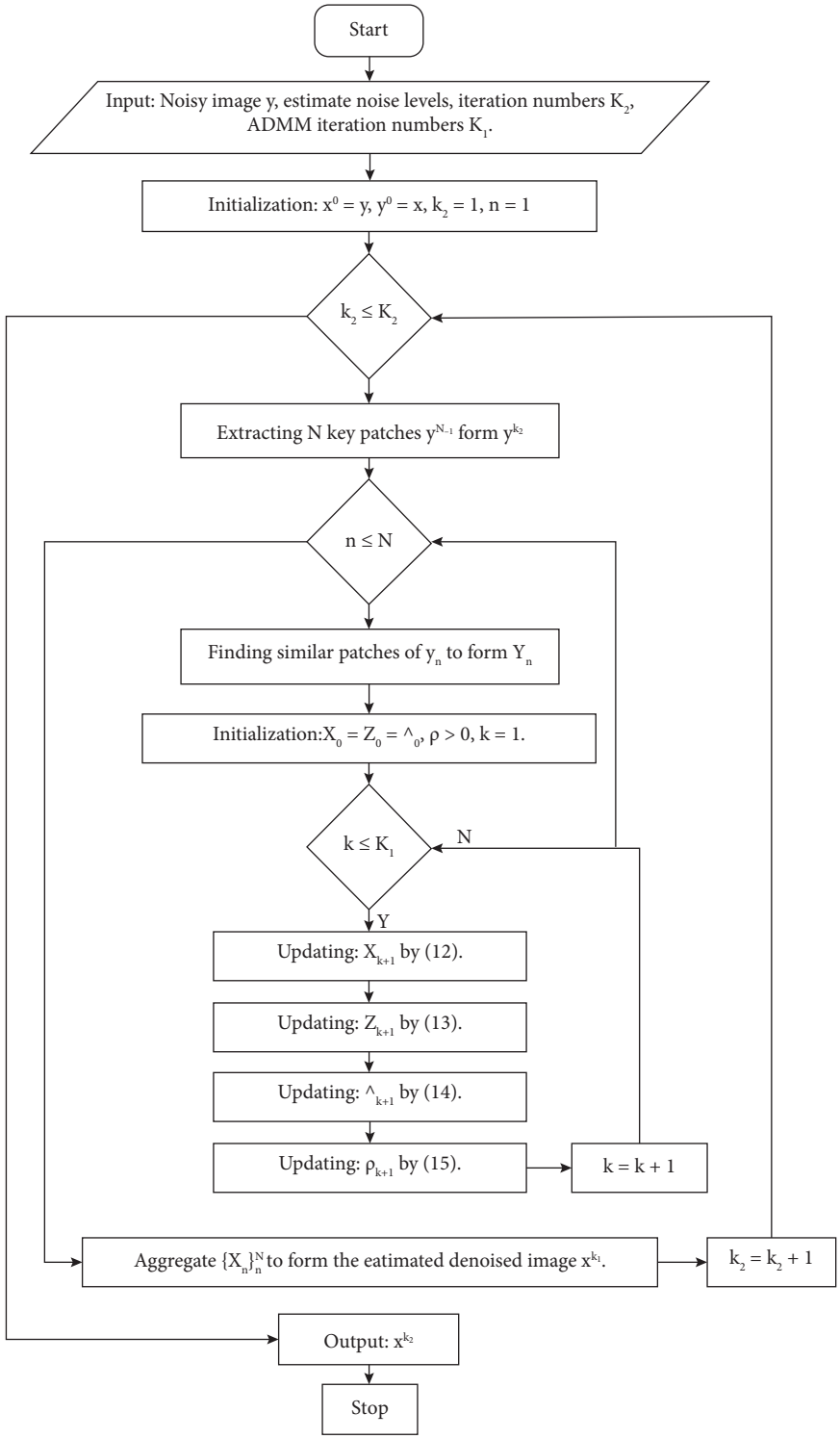

Figure 1: The flowchart of our algorithm.

Input: Noisy matrix $\mathbf{Y}$, weight matrix $\mathbf{W}_1, \mathbf{W}_2$, $\mu > 1$, iteration threshold K_1;
Initialize: $\mathbf{X}_0 = \mathbf{Z}_0 = \mathbf{\Lambda}_0 = \mathbf{0}, \rho_0 > 0, k = 0$, isStop = False;
(1) **while** isStop = = False **do**
(2) update $\mathbf{X}$ by (12);
(3) update $\mathbf{Z}$ by (13);
(4) update $\mathbf{\Lambda}$ by (14);
(5) update ρ by (15);
(6) k $\longleftarrow$ $k+1$;
(7) **end while**
(8) **if** (Convergence criterion is satisfied) && ($k \le K_1$) **then**
(9) isStop $\longleftarrow$ True;
(10) **end if**
Output: Denoised patch $\mathbf{X}^*$.

Algorithm 2: Solving multi-weighted Schatten p-norm minimization via ADMM.

$$\begin{aligned}
&\left\|\mathbf{W_1}(\mathbf{Y}-\mathbf{X_k})\mathbf{W_2}\right\|_F^2+\left\|\mathbf{Z_k}\right\|_{\mathbf{w},S_p}^p \\
&\quad=\mathscr{L}(\mathbf{X}_k,\mathbf{Z}_k,\mathbf{\Lambda}_{k-1},\rho_{k-1})-\langle\mathbf{\Lambda}_{k-1},\mathbf{X}_k-\mathbf{Z}_k\rangle-\frac{\rho_{k-1}}{2}\left\|\mathbf{X_k}-\mathbf{Z_k}\right\|_F^2 \\
&\quad=\mathscr{L}(\mathbf{X}_k,\mathbf{Z}_k,\mathbf{\Lambda}_{k-1},\rho_{k-1})-\langle\mathbf{\Lambda}_{k-1},\frac{(\mathbf{\Lambda}_k-\mathbf{\Lambda}_{k-1})}{\rho_{k-1}}\rangle-\frac{\rho_{k-1}}{2}\left\|\frac{\mathbf{\Lambda_k}-\mathbf{\Lambda_{k-1}}}{\boldsymbol{\rho}_{\mathbf{k-1}}}\right\|_F^2 \\
&\quad=\mathscr{L}(\mathbf{X}_k,\mathbf{Z}_k,\mathbf{\Lambda}_{k-1},\rho_{k-1})+\frac{\left\|\mathbf{\Lambda_{k-1}}\right\|_F^2-\left\|\mathbf{\Lambda_k}\right\|_F^2}{2\rho_{k-1}}.
\end{aligned} \tag{26}$$

Since $\mathscr{L}(\mathbf{X}_k,\mathbf{Z}_k,\mathbf{\Lambda}_{k-1},\rho_{k-1})$ and $\{\mathbf{\Lambda_k}\}$ are upper bounded, the sequence $\{\mathbf{W}_1(\mathbf{Y}-\mathbf{X}_k)\mathbf{W}_2\}$ and $\mathbf{Z}_k$ are also bounded. Since $\mathbf{X}_{k+1}=\mathbf{Z}_{k+1}+(\mathbf{\Lambda}_{k+1}-\mathbf{\Lambda}_k)/\rho_k$, we can deduce that the sequence $\{\mathbf{X}_k\}$ is upper bounded as well. As a result, $\{\mathbf{X}_k,\mathbf{Z}_k\}$ have at least one accumulation point. Then, we obtain

$$\lim_{k\longrightarrow+\infty}\left\|\mathbf{X_{k+1}}-\mathbf{Z_{k+1}}\right\|_F=\lim_{k\longrightarrow+\infty}\frac{1}{\rho_k}\left\|\mathbf{\Lambda_{k+1}}-\mathbf{\Lambda_k}\right\|_F=0. \tag{27}$$

Consequently, the convergence criterion of equation (a) is proved.

(4) In the fourth step, we prove the convergence criterion of equation (b). As defined in Section 3.3 and $\mathbf{X}_k=1/\rho_{k-1}(\mathbf{\Lambda}_k-\mathbf{\Lambda}_{k-1})+\mathbf{Z}_k$, we have

$$\begin{aligned}
&\lim_{k\longrightarrow\infty}\left\|\mathbf{X}_{k+1}-\mathbf{X}_k\right\|_F \\
&=\lim_{k\longrightarrow\infty}\left\|\mathrm{vec}^{-1}\left(\left(\mathbf{I}_M\otimes\mathbf{A}+\mathbf{B}^T\otimes\mathbf{I}_{3p^2}\right)^{-1}\mathrm{vec}(\mathbf{C})\right)-\rho_{k-1}^{-1}(\mathbf{\Lambda}_k-\mathbf{\Lambda}_{k-1})-\mathbf{Z}_k\right\|_F
\end{aligned}$$

$$
\begin{aligned}
&= \lim_{k\longrightarrow\infty} \left\| \mathrm{vec}^{-1}\left(\left(\mathbf{I}_M \otimes \mathbf{A} + \mathbf{B}^T \otimes \mathbf{I}_{3p^2}\right)^{-1} \mathrm{vec}\left(\mathbf{W}_1^\top \mathbf{W}_1 \mathbf{Y}_k - \mathbf{W}_1^\top \mathbf{W}_1 \mathbf{Z}_k + \left(\frac{\boldsymbol{\rho}_\mathbf{k}}{2}\mathbf{Z}_\mathbf{k} - \frac{\mathbf{1}}{2}\boldsymbol{\Lambda}_\mathbf{k}\right)\left(\mathbf{W}_2\mathbf{W}_2^\mathbf{T}\right)^{-\mathbf{1}}\right)\right) - \boldsymbol{\rho}_{\mathbf{k-1}}^{-\mathbf{1}}\left(\boldsymbol{\Lambda}_\mathbf{k} - \boldsymbol{\Lambda}_{\mathbf{k-1}}\right)\right\|_F \\
&\leq \lim_{k\longrightarrow\infty} \left\| \mathrm{vec}^{-1}\left(\left(\mathbf{I}_M \otimes \left(\mathbf{W}_1\mathbf{W}_1^\top\right) + \left(\frac{\rho_k}{2}\left(\left(\mathbf{W}_2\mathbf{W}_2^\top\right)^{-1}\right)^T \otimes \mathbf{I}_{3p^2}\right)\right)^{-1} \mathrm{vec}\left(\mathbf{W}_1^\top \mathbf{W}_1 \mathbf{Y}_k + \mathbf{W}_1^\top \mathbf{W}_1 \mathbf{Z}_\mathbf{k}\left(\frac{\boldsymbol{\rho}_\mathbf{k}}{2}\mathbf{Z}_\mathbf{k} - \frac{\mathbf{1}}{2}\boldsymbol{\Lambda}_\mathbf{k}\right)\left(\mathbf{W}_2\mathbf{W}_2^\mathbf{T}\right)^{-\mathbf{1}}\right)\right) + \boldsymbol{\rho}_{\mathbf{k-1}}^{-\mathbf{1}}\left(\boldsymbol{\Lambda}_\mathbf{k} - \boldsymbol{\Lambda}_{\mathbf{k-1}}\right)\right\|_F \\
&= 0.
\end{aligned}
\tag{28}
$$

(5) At last, we prove the convergence criterion of equation (c).

$$
\begin{aligned}
\lim_{k\longrightarrow\infty} \left\|\mathbf{Z}_{\mathbf{k+1}} - \mathbf{Z}_\mathbf{k}\right\|_F &= \lim_{k\longrightarrow\infty} \left\|\boldsymbol{\rho}_\mathbf{k}^{-\mathbf{1}}\boldsymbol{\Lambda}_\mathbf{k} - \boldsymbol{\rho}_\mathbf{k}^{-\mathbf{1}}\boldsymbol{\Lambda}_{\mathbf{k+1}} + \mathbf{X}_{\mathbf{k+1}} - \mathbf{Z}_\mathbf{k}\right\|_F \\
&= \lim_{k\longrightarrow\infty} \left\|\mathbf{X}_k + \rho_{k-1}^{-1}\boldsymbol{\Lambda}_{k-1} - \mathbf{Z}_k + \mathbf{X}_{k+1}\right. \\
&\quad \left. - \mathbf{X}_k - \rho_{k-1}^{-1}\boldsymbol{\Lambda}_{k-1} + \rho_k^{-1}\boldsymbol{\Lambda}_k - \rho_k^{-1}\boldsymbol{\Lambda}_{k+1}\right\|_F \\
&\leq \lim_{k\longrightarrow\infty} \left\|\sum_i \rho_{k-1}^{-1} J w_i\right\|_F + \left\|\mathbf{X}_{k+1} - \mathbf{X}_k\right\| \\
&\quad + \left\|\rho_{k-1}^{-1}\boldsymbol{\Lambda}_{k-1} - \rho_k^{-1}\boldsymbol{\Lambda}_k + \rho_k^{-1}\mathbf{L}_{k+1}\right\|_F \\
&= 0.
\end{aligned}
\tag{29}
$$

This completes the proof of Theorem 1.

Theorem 1 explains that the sequences of variables generated by Algorithm 2 are bounded and converge to their respective stationary points. Consequently, the convergence of Algorithm 2 can be established. □

4. Experimental Results

In our study, we conduct an extensive evaluation of the proposed model on three real noisy color image datasets. To assess the effectiveness of our proposed model, we compared it with seven state-of-the-art models, including CBM3D [46], MCWNNM [20], MCWSNM [21], Denoising Convolutional Neural Network (DnCNN) [13], Fast and Flexible Denoising Network (FFDNet) [24], Guided Image Denoising (GID) [51], and Neat Image (NI) [52]. Notably, all experiments (except NI) are conducted on a desktop computer running MATLAB R2020a, with a Windows 11 operating system, 2.90 GHz Intel i7-10700 CPU, and 16 GB RAM. Meanwhile, NI uses the latest release version available on its official website, and the experiments are implemented in standalone software on the same device.

The next content is organized as follows. In Section 4.1, we present the details of the three used real color image datasets, and the evaluation criteria of the denoised image are discussed in Section 4.2. Then, we present the parameter settings of the proposed algorithm in Section 4.3. Finally, in Section 4.4, we show the denoised results of all compared experiments.

4.1. Description of Datasets. Obtaining ground-truth data for a dataset of real color images can be challenging due to the unavoidable noise generated during the image acquisition process. Currently, one of the most widely used methods for generating ground-truth is to capture multiple photos of the same scene under different camera settings and lighting conditions and then average them to produce a high-quality image that serves as the ground truth.

In order to evaluate the performance of image denoising, we utilize three widely recognized and commonly used color image datasets. Each of these datasets is distinct in its characteristics and presents unique challenges for denoising algorithms. The detailed description of these datasets is as follows.

(1) Dataset 1: The Noise Clinic (https://www.ipol.im/pub/art/2015/125/) dataset [47] comprises numerous realistic noise images captured in an uncontrolled outdoor environment, featuring both gray and color images. In our experiments, we selected 12 real color images, as illustrated in Figure 2, and cropped them into squares of equal size. However, it should be noted that this dataset does not have a ground-truth reference.

(2) Dataset 2: To improve the training of their model, the authors in [53] created a real image dataset (http://snam.ml/research/ccnoise), comprising 11 indoor scenes, with 500 images each. To obtain noise-free images, the authors computed the mean image of

Figure 2: The scene of dataset 1: the 12 test images cropped from NC12 dataset.

each scene as the ground truth. Due to the large size of the original images (7360×4912 pixels), the dataset was cropped to 15 smaller images with a size of 512×512 for the experiment. This dataset is available in PNG format and includes generated ground-truth references for evaluation purposes.

(3) Dataset 3: The PolyU (https://github.com/csjunxu/PolyU-Real-World-Noisy-Images-Dataset) dataset [54] is a sizable repository of real-world noisy images, each of which has been paired with a reasonably obtained corresponding "ground-truth" image. Similar to dataset 2, the fundamental concept of this dataset is to capture a constant scene multiple times and generate a mean image to be the approximate representation of the ground truth. This dataset is available in JPG format with a size of 512×512.

By utilizing these datasets, we can comprehensively evaluate the performance of our image denoising method and compare it with other state-of-the-art denoising approaches.

4.2. Assessment Criteria for Denoising Results. We evaluate the efficacy of denoising methods using two widely used standards: peak signal-to-noise ratio (PSNR) and structural similarity index (SSIM), which are defined in equations (30) and (31). Higher PSNR and SSIM values indicate a better denoising performance in comparison to the approximated ground truth. However, it should be noted that for dataset 1, the evaluation can only be based on visual inspection due to the unavailability of the ground truth.

$$\mathrm{PSNR}(\mathbf{x},\mathbf{y}) = 10 \times \log_{10}\left(\frac{\mathbf{MAX}_I^2}{\mathbf{MSE}(\mathbf{x},\mathbf{y})}\right), \tag{30}$$

$$\mathrm{SSIM}(\mathbf{x},\mathbf{y}) = \frac{\left(2\mu_{\mathbf{x}}\mu_{\mathbf{y}} + c_1\right)\left(2\sigma_{\mathrm{xy}} + c_2\right)}{\left(\mu_{\mathbf{x}}^2 + \mu_{\mathbf{y}}^2 + c_1\right)\left(\sigma_{\mathbf{x}}^2 + \sigma_{\mathbf{y}}^2 + c_2\right)}, \tag{31}$$

where

$$\mathbf{MSE}(\mathbf{x},\mathbf{y}) = \frac{1}{\mathrm{mn}} \sum_{i=0}^{m-1} \sum_{j=0}^{n-1} \left[\mathbf{x}_{i,j} - \mathbf{y}_{i,j}\right]^2, \tag{32}$$

is the mean square error of $\mathbf{x}$ and $\mathbf{y}$. $\mathbf{MAX}_I$ is the maximum possible pixel value for the image. For the color image in our experiments, the value is set to 255. $\mathbf{x}, \mathbf{y}$ denotes the pixel value matrix of clean image and denoised image with size of $m \times n$. μ_x, μ_y and $\sigma_{\mathbf{x}}^2, \sigma_{\mathbf{y}}^2$ are mean value and variance of $\mathbf{x}$ and $\mathbf{y}$, respectively. σ_{xy} is the covariance of $\mathbf{x}$ and $\mathbf{y}$.

4.3. Experimental Settings. The crucial parameters in our method are configured as follows. Specifically, for dataset 1, we set the number of iterations $K_2 = 1$, while $K_2 = 2$ for the second and third datasets. Additionally, the parameter p for the weighted Schatten p-norm is set to $p = 0.9$ and $p = 0.99$ for the first and second/third datasets, respectively. The remaining parameters are maintained consistently across all datasets, where the patch size is 7×7, the number of iterations $K_1 = 10$, the size of the search window is 40×40, the number of similar patches is $M = 70$, the constant for the weight vector $c = 2\sqrt{2}$, and the updating parameter μ is set to 1.001.

Apart from NI, which is a standalone software program, all other denoising methods require the input noise level to be specified. In the experiments, we utilize Chen's method [45] to predict the noise level of the real image, which is then used as input to the denoising methods. For methods such as CBM3D that only require a single noise level, we set this value as $\sigma = \sqrt{\mathrm{mean}(\sigma_r^2, \sigma_g^2, \sigma_b^2)}$. Regarding the noise standard deviation of patches in our algorithm, we initialize it as $\sigma_m = \sigma$ and then update it using the following equation:

$$\sigma_m = \sqrt{\max\left(0, \sigma^2 - \left\|\mathbf{y}_m - \mathbf{x}_m\right\|_2^2\right)}, \tag{33}$$

where $\|\cdot\|_2$ is the Euclidean norm.

4.4. Experiments on the Real Noise Datasets. Due to the lack of ground truth, we can only judge the denoising effect of the methods from the visual inspection in dataset 1. Figure 3 presents the "frog" image from dataset 1, which is contaminated by near-uniform, slight noise. From the results, we can observe that all algorithms except NI demonstrate significant denoising effects. DnCNN, FFDNet, CBM3D, and GID show some remaining noise residue, while MCWSNM results in a loss of image details. In contrast, MCWNNM and our proposed algorithm produce superior visual results with minimal noise residue. Figure 4 illustrates the "dog" image from Dataset 1. The visual results in Figure 4 indicate that CBM3D, GID, DnCNN, FFDNet, and NI exhibit noticeable noise residuals. MCWSNM sacrifices some of the image details in

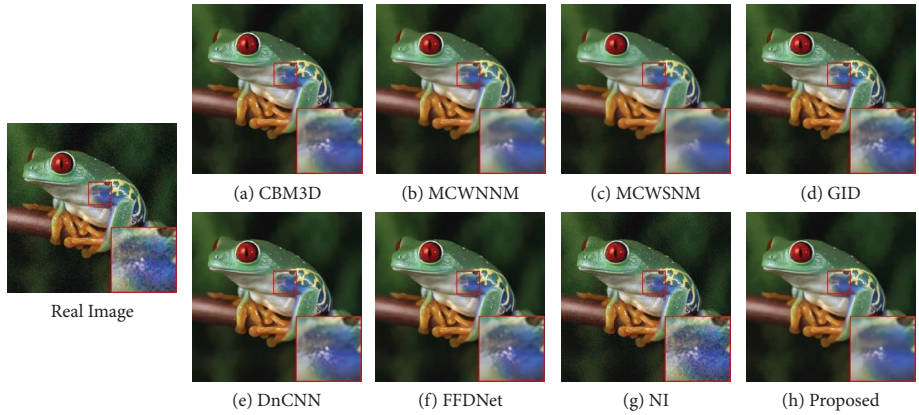

Figure 3: Denoised images of the real noisy image "frog" in dataset 1 by different methods. The ground truth of the noisy input is not available.

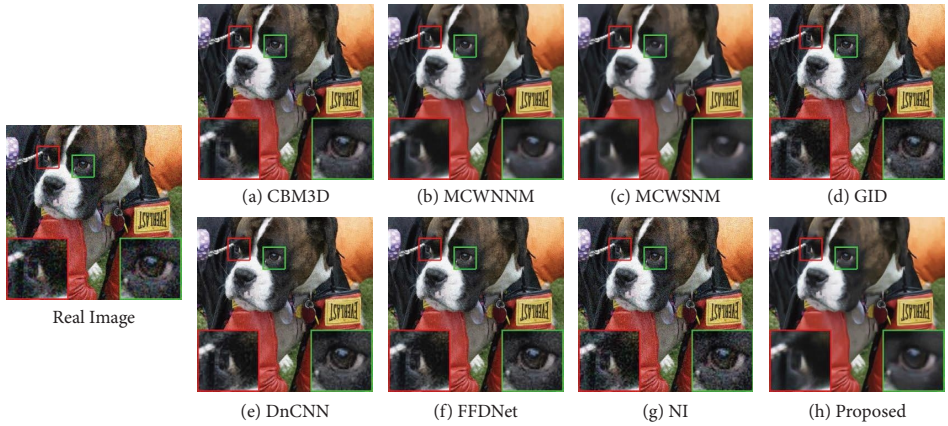

Figure 4: Denoised images of the real noisy image "dog" in dataset 1 by different methods. The ground truth of the noisy input is not available.

the eye area, and MCWNNM overly smooths the image. In contrast, our proposed method obtains the best visual results with abundant details.

Figure 5 displays an image captured by a Canon 5D camera with ISO = 3200. It is evident from the results that CBM3D, DnCNN, and FFDNet failed to effectively remove the noise. NI just removes a small part of the noise. GID removes most of the noise, while a small portion of noise still remained. Though MCWNNM and MCWSNM manage to attain respectable denoising outcomes, they compromise texture details noticeably. In contrast, our proposed algorithm secures the highest numerical results, successfully eliminating noise while simultaneously conserving a higher degree of intricate details. Figure 6 depicts the image captured by Nikon D800. The results show that CBM3D, NI, DnCNN, and FFDNet did not achieve satisfactory denoising results. In addition, GID yields a blurring effect. In comparison, while the denoising outcomes of MCWNNM and MCWSNM are commendable, they encounter challenges in recovering intricate details. Conversely, our algorithm excels in both detail recovery and denoising effectiveness, yielding the highest PSNR value.

The comparison of denoising methods on datasets 2 and 3 is facilitated by the availability of ground truth, enabling numerical evaluation of their performance. Tables 1 and 2 present the PSNR and SSIM values of the competing models, respectively, with the highest values highlighted in bold. It can be seen that our proposed model outperforms other models in terms of PSNR and SSIM for most images in both datasets. However, it should be noted that FFDNet, which is designed as a deep neural network for color image denoising, does not perform well on both datasets, indicating that neural network methods can be overly reliant on the training dataset. Additionally, NI, a commercial software program, exhibits varying levels of denoising performance across different images. CBM3D and DnCNN, on the other hand, are methods specially designed to remove AWGN noise and are therefore not well suited for denoising real color images. GID is a denoising method tailored for real color images, but its performance only outperforms other models on a few images. The most similar models to our proposed method are MCWNNM and MCWSNM, and the experimental results demonstrate that by considering the noise differences between different patches, superior denoising performance can be achieved.

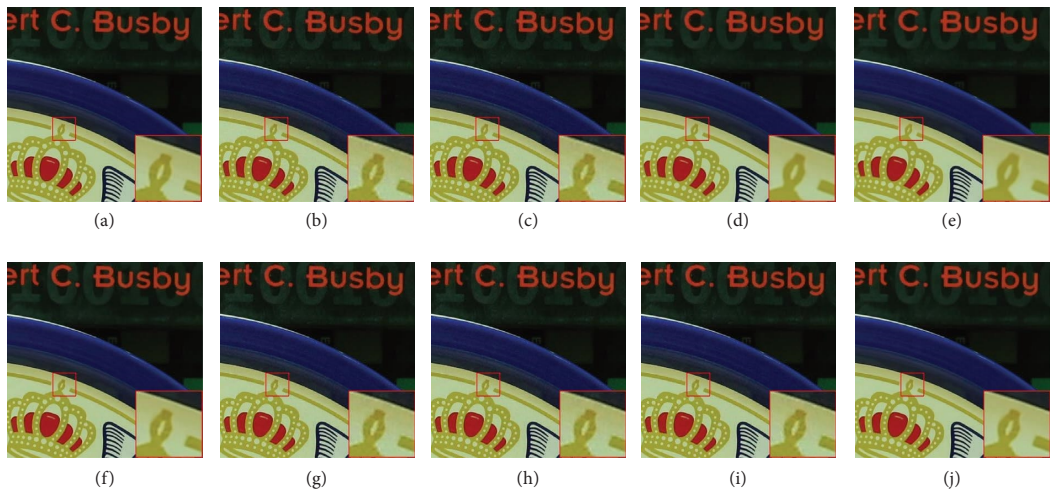

Figure 5: Denoised images of the real noisy image (Canon 5D (1)) in dataset 2 by different methods. (a) Mean image Canon 5D. (b) Real image (noised). (c) CBM3D PSNR: 37.002 dB. (d) MCWNNM PSNR: 41.201 dB. (e) MCWSNM PSNR: 41.220 dB. (f) GID PSNR: 40.817 dB. (g) DnCNN PSNR: 37.624 dB. (h) FFDNet PSNR: 37.627 dB. (i) NI PSNR: 38.384 dB. (j) Proposed PSNR: **41.395** dB.

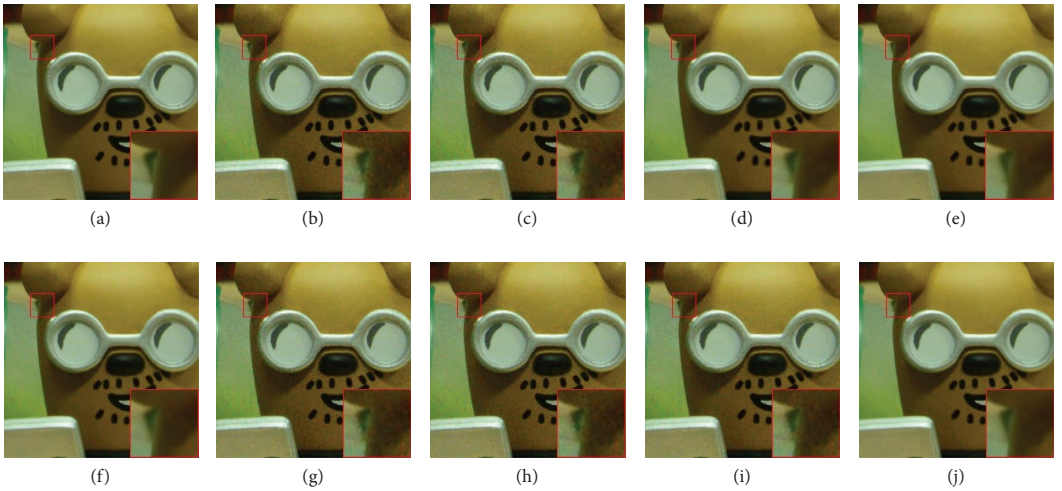

Figure 6: Denoised images of the real noisy image (Nikon D500) by different methods. (a) Mean image Nikon D800. (b) Real image (noised). (c) CBM3D PSNR: 33.816 dB. (d) MCWNNM PSNR: 39.190 dB. (e) MCWSNM PSNR: 39.092 dB. (f) GID PSNR: 38.545 dB. (g) DnCNN PSNR: 33.930 dB. (h) FFDNet PSNR: 33.874 dB. (i) NI PSNR: 34.124 dB. (j) Proposed PSNR: **39.323** dB.

Table 1: PSNR (dB) and SSIM results of all competing models on dataset 2.

Image	CBM3D	MCWNNM	MCWSNM	GID	DnCNN	FFDNet	NI	Proposed
PSNR								
Canon 5D (3)	34.502	36.480	36.985	36.924	34.651	34.599	35.660	**37.022**
Nikon D600 (6)	35.313	39.563	39.526	38.675	35.431	35.384	39.090	**39.728**
Nikon D800 (9)	35.246	**39.539**	39.390	39.198	35.358	35.302	38.817	39.391
Nikon D800 (12)	33.284	39.416	39.519	37.643	33.359	33.338	38.384	**39.754**
Nikon D800 (15)	30.059	**33.965**	33.777	32.961	30.125	30.113	32.590	33.944
Average	33.681	37.793	37.840	37.080	33.785	33.747	36.908	**37.968**
SSIM								
Canon 5D (3)	0.9346	0.9634	0.9670	**0.9687**	0.9367	0.9350	0.9546	0.9683
Nikon D600 (6)	0.8721	0.9711	0.9710	0.9624	0.8740	0.8747	0.9550	**0.9720**
Nikon D800 (9)	0.8693	0.9561	**0.9564**	0.9532	0.8729	0.8714	0.9368	**0.9564**
Nikon D800 (12)	0.7874	0.9591	0.9599	0.9382	0.7909	0.7898	0.9275	**0.9616**
Nikon D800 (15)	0.7939	**0.9215**	0.9167	0.8980	0.7974	0.7963	0.8827	0.9205
Average	0.8515	0.9542	0.9542	0.9441	0.8544	0.8534	0.9313	**0.9558**

The first column of the table represents the camera settings.

Table 2: PSNR (dB) and SSIM results of all competing models on dataset 3.

Image	CBM3D	MCWNNM	MCWSNM	GID	DnCNN	FFDNet	NI	Proposed
PSNR								
Canon 5D (1)	39.448	40.908	40.867	**40.910**	39.351	39.344	40.631	40.897
Canon 80D (30)	37.616	40.654	40.710	40.100	37.605	37.614	40.449	**40.832**
Canon 600D (45)	38.177	41.488	**41.825**	41.577	38.145	38.129	37.480	41.754
Nikon D800 (60)	39.122	41.762	41.785	41.786	39.113	39.065	37.223	**41.810**
Sony A7 II (90)	37.989	**40.074**	39.966	39.599	38.043	38.030	39.260	39.884
Sony A7 II (100)	34.782	39.701	39.504	39.130	34.905	34.806	38.491	**39.839**
Average	37.856	40.764	40.776	39.497	35.866	35.780	38.922	**40.836**
SSIM								
Canon 5D (1)	0.9582	**0.9808**	0.9805	0.9806	0.9561	0.9559	0.9773	0.9807
Canon 80D (30)	0.9225	0.9719	0.9722	0.9722	0.9222	0.9221	0.9649	**0.9727**
Canon 600D (45)	0.9206	0.9743	0.9750	**0.9757**	0.9205	0.9195	0.9701	0.9747
Nikon D800 (60)	0.9464	0.9818	0.9818	**0.9824**	0.9460	0.9451	0.9711	0.9819
Sony A7 II (90)	0.9253	0.9572	0.9569	0.9554	0.9247	0.9263	0.9450	**0.9573**
Sony A7 II (100)	0.8681	0.9734	0.9729	0.9724	0.8697	0.8660	0.9525	**0.9741**
Average	0.9235	0.9732	0.9732	0.9647	0.8833	0.8813	0.9635	**0.9736**

The first column of the table represents the camera settings.

5. Conclusion

The noise distribution in real-world images varies not only between color channels but also spatially within each patch. Building upon this observation, in this paper, we proposed a new real-world color image denoising model. The model employed a multi-weighted strategy to denoise images by utilizing nonconvex weighted Schatten p-norm minimization. Specifically, a new weight matrix was introduced into MCWSNM to balance noise differences between patches. Since the proposed model is nonconvex, and without an analytical solution, we developed an accurate and efficient optimization algorithm based on ADMM framework to solve the proposed model. In addition, the theoretical convergence analysis of the optimization algorithm was also provided. Finally, the experiments on three real-world noisy image datasets demonstrated superior performance of the proposed model compared to state-of-the-art methods. In our future work, we will focus on modeling more complex statistical properties of noise and further improving real-world color image denoising.

Data Availability

The data used to support the findings of this study can be obtained from the following websites: https://www.ipol.im/pub/art/2015/125/; http://snam.ml/research/ccnoise; and https://github.com/csjunxu/PolyU-Real-World-Noisy-Images-Dataset.

Conflicts of Interest

The authors declare that they have no conflicts of interest.

Acknowledgments

This study was supported by the Natural Science Foundation of Ningxia (grant/award number: 2020AAC03254).

References

[1] S. Alexander, "Image acquisition and quality in digital radiography," *Radiologic Technology*, vol. 88, no. 1, pp. 53–66, 2016.

[2] T. H. Chan, K. Jia, S. Gao, J. Lu, Z. Zeng, and Y. Ma, "PCANet: a simple deep learning baseline for image classification?" *IEEE Transactions on Image Processing*, vol. 24, no. 12, pp. 5017–5032, 2015.

[3] F. Wang, M. Jiang, C. Qian et al., "Residual attention network for image classification," in *Proceedings of the IEEE conference on computer vision and pattern recognition*, pp. 3156–3164, Honolulu, HI, USA, July 2017.

[4] L. C. Chen, Y. Yang, J. Wang, W. Xu, and A. L. Yuille, "Attention to scale: scale-aware semantic image segmentation," in *Proceedings of the IEEE conference on computer vision and pattern recognition*, pp. 3640–3649, Las Vegas, NV, USA, June 2016.

[5] V. Badrinarayanan, A. Kendall, and R. Cipolla, "Segnet: a deep convolutional encoder-decoder architecture for image segmentation," *IEEE Transactions on Pattern Analysis and Machine Intelligence*, vol. 39, no. 12, pp. 2481–2495, 2017.

[6] K. He, X. Zhang, S. Ren, and J. Sun, "Deep residual learning for image recognition," in *Proceedings of the IEEE conference on computer vision and pattern recognition*, pp. 770–778, Las Vegas, NV, USA, June 2016.

[7] B. Zoph, V. Vasudevan, J. Shlens, and Q. V. Le, "Learning transferable architectures for scalable image recognition," in *Proceedings of the IEEE conference on computer vision and pattern recognition*, pp. 8697–8710, Salt Lake City, UT, USA, August 2018.

[8] M. Kivanc Mihcak, I. Kozintsev, K. Ramchandran, and P. Moulin, "Low-complexity image denoising based on statistical modeling of wavelet coefficients," *IEEE Signal Processing Letters*, vol. 6, no. 12, pp. 300–303, 1999.

[9] A. Buades, B. Coll, and J. M. Morel, "A non-local algorithm for image denoising," in *2005 IEEE computer society conference on computer vision and pattern recognition (CVPR'05)*, vol. 2, pp. 60–65, Ieee, San Diego, CA, USA, June 2005.

[10] M. Elad and M. Aharon, "Image denoising via sparse and redundant representations over learned dictionaries," *IEEE Transactions on Image Processing*, vol. 15, no. 12, pp. 3736–3745, 2006.

[11] K. Dabov, A. Foi, V. Katkovnik, and K. Egiazarian, "Image restoration by sparse 3D transform-domain collaborative filtering," in *Image Processing: Algorithms and Systems VI*, vol. 6812, pp. 62–73, SPIE, San Jose, CA, USA, March 2008.

[12] S. Gu, L. Zhang, W. Zuo, and X. Feng, "Weighted nuclear norm minimization with application to image denoising," in *Proceedings of the IEEE conference on computer vision and pattern recognition*, pp. 2862–2869, Columbus, OH, USA, June 2014.

[13] K. Zhang, W. Zuo, Y. Chen, D. Meng, and L. Zhang, "Beyond a Gaussian denoiser: residual learning of deep cnn for image denoising," *IEEE Transactions on Image Processing*, vol. 26, no. 7, pp. 3142–3155, 2017.

[14] J. Xu, L. Zhang, and D. Zhang, "A trilateral weighted sparse coding scheme for real-world image denoising," in *Proceedings of the European conference on computer vision (ECCV)*, pp. 20–36, Munich, Germany, October 2018.

[15] C. Knaus and M. Zwicker, "Progressive image denoising," *IEEE Transactions on Image Processing*, vol. 23, no. 7, pp. 3114–3125, 2014.

[16] J. Mairal, F. Bach, J. Ponce, G. Sapiro, and A. Zisserman, "Non-local sparse models for image restoration," in *2009 IEEE 12th international conference on computer vision IEEE*, pp. 2272–2279, Kyoto, Japan, September 2009.

[17] W. Dong, L. Zhang, G. Shi, and X. Li, "Nonlocally centralized sparse representation for image restoration," *IEEE Transactions on Image Processing*, vol. 22, no. 4, pp. 1620–1630, 2013.

[18] J. Zhang, D. Zhao, and W. Gao, "Group-based sparse representation for image restoration," *IEEE Transactions on Image Processing*, vol. 23, no. 8, pp. 3336–3351, 2014.

[19] W. Dong, G. Shi, and X. Li, "Nonlocal image restoration with bilateral variance estimation: a low-rank approach," *IEEE Transactions on Image Processing*, vol. 22, no. 2, pp. 700–711, 2013.

[20] J. Xu, L. Zhang, D. Zhang, and X. Feng, "Multi-channel weighted nuclear norm minimization for real color image denoising," in *Proceedings of the IEEE international conference on computer vision*, pp. 1096–1104, Venice, Italy, October 2017.

[21] X. Huang, B. Du, and W. Liu, "Multichannel color image denoising via weighted schatten p-norm minimization," in *Proceedings of the Twenty-Ninth International Conference on International Joint Conferences on Artificial Intelligence*, Montreal, Canada, pp. 637–644, September 2021.

[22] Y. Su, Z. Li, H. Yu, and Z. Wang, "Multi-band weighted lp norm minimization for image denoising," *Information Sciences*, vol. 537, pp. 162–183, 2020.

[23] Y. Chen and T. Pock, "Trainable nonlinear reaction diffusion: a flexible framework for fast and effective image restoration," *IEEE Transactions on Pattern Analysis and Machine Intelligence*, vol. 39, no. 6, pp. 1256–1272, 2017.

[24] K. Zhang, W. Zuo, and L. Zhang, "FFDNet: toward a fast and flexible solution for CNN-based image denoising," *IEEE Transactions on Image Processing*, vol. 27, no. 9, pp. 4608–4622, 2018.

[25] S. Lefkimmiatis, "Universal denoising networks: a novel CNN architecture for image denoising," in *Proceedings of the IEEE conference on computer vision and pattern recognition*, pp. 3204–3213, Salt Lake City, UT, USA, June 2018.

[26] S. Guo, Z. Yan, K. Zhang, W. Zuo, and L. Zhang, "Toward convolutional blind denoising of real photographs," in *Proceedings of the IEEE/CVF conference on computer vision and pattern recognition*, pp. 1712–1722, Long Beach, CA, USA, June 2019.

[27] S. Anwar and N. Barnes, "Real image denoising with feature attention," in *Proceedings of the IEEE/CVF international conference on computer vision*, pp. 3155–3164, Seoul, Republic of Korea, October 2019.

[28] B. Wen, Y. Li, and Y. Bresler, "When sparsity meets low-rankness: transform learning with non-local low-rank constraint for image restoration," in *2017 IEEE international conference on acoustics, speech and signal processing (ICASSP)*, pp. 2297–2301, IEEE, New Orleans, LA, USA, March 2017.

[29] D. Liu, B. Wen, X. Liu, Z. Wang, and T. S. Huang, "When image denoising meets high-level vision tasks: a deep learning approach," in *Proceedings of the 27th International Joint Conference on Artificial Intelligence*, pp. 842–848, Stockholm, Sweden, July 2018.

[30] Z. Wang, Y. Liu, X. Luo, J. Wang, C. Gao, and D. Peng, "Large-scale affine matrix rank minimization with a novel nonconvex regularizer," *IEEE Transactions on Neural Networks and Learning Systems*, vol. 33, no. 9, pp. 4661–4675, 2022.

[31] Z. Wang, W. Wang, J. Wang, and S. Chen, "Fast and efficient algorithm for matrix completion via closed-form 2/3-thresholding operator," *Neurocomputing*, vol. 330, pp. 212–222, 2019.

[32] Z. Wang, C. Gao, X. Luo, M. Tang, J. Wang, and W. Chen, "Accelerated inexact matrix completion algorithm via closed-form q-thresholding (q = 1/2, 2/3) operator," *International Journal of Machine Learning and Cybernetics*, vol. 11, no. 10, pp. 2327–2339, 2020.

[33] Z. Wang, D. Hu, X. Luo, W. Wang, J. Wang, and W. Chen, "Performance guarantees of transformed schatten-1 regularization for exact low-rank matrix recovery," *International Journal of Machine Learning and Cybernetics*, vol. 12, pp. 3379–3395, 2021.

[34] Z. Liu, D. Hu, Z. Wang, J. Gou, and T. Jia, "LatLRR for subspace clustering via reweighted Frobenius norm minimization," *Expert Systems with Applications*, vol. 224, Article ID 119977, 2023.

[35] Y. Xie, S. Gu, Y. Liu, W. Zuo, W. Zhang, and L. Zhang, "Weighted schatten p-norm minimization for image denoising and background subtraction," *IEEE Transactions on Image Processing*, vol. 25, no. 10, pp. 4842–4857, 2016.

[36] Y. Shan, D. Hu, Z. Wang, and T. Jia, "Multi-channel nuclear norm minus Frobenius norm minimization for color image denoising," *Signal Processing*, vol. 207, Article ID 108959, 2023.

[37] Y. Chen, X. Xiao, and Y. Zhou, "Low-rank quaternion approximation for color image processing," *IEEE Transactions on Image Processing*, vol. 29, pp. 1426–1439, 2020.

[38] T. Liu, D. Hu, Z. Wang, J. Gou, and W. Chen, "Hyperspectral image denoising using nonconvex fraction function," *IEEE Geoscience and Remote Sensing Letters*, vol. 20, pp. 1–5, 2023.

[39] J. F. Cai, E. J. Candès, and Z. Shen, "A singular value thresholding algorithm for matrix completion," *SIAM Journal on Optimization*, vol. 20, no. 4, pp. 1956–1982, 2010.

[40] E. J. Candès, X. Li, Y. Ma, and J. Wright, "Robust principal component analysis?" *Journal of the ACM*, vol. 58, no. 3, pp. 1–37, 2011.

[41] N. Yair and T. Michaeli, "Multi-scale weighted nuclear norm image restoration," in *Proceedings of the IEEE conference on*

computer vision and pattern recognition, pp. 3165–3174, Salt Lake City, UT, USA, June 2018.

[42] Y. Yu, Y. Zhang, and S. Yuan, "Quaternion-based weighted nuclear norm minimization for color image denoising," *Neurocomputing*, vol. 332, pp. 283–297, 2019.

[43] S. Pyatykh, J. Hesser, and L. Zheng, "Image noise level estimation by principal component analysis," *IEEE Transactions on Image Processing*, vol. 22, no. 2, pp. 687–699, 2013.

[44] X. Liu, M. Tanaka, and M. Okutomi, "Single-image noise level estimation for blind denoising," *IEEE Transactions on Image Processing*, vol. 22, no. 12, pp. 5226–5237, 2013.

[45] G. Chen, F. Zhu, and P. Ann Heng, "An efficient statistical method for image noise level estimation," in *Proceedings of the IEEE International Conference on Computer Vision*, pp. 477–485, Santiago, Chile, December 2015.

[46] K. Dabov, A. Foi, V. Katkovnik, and K. Egiazarian, "Color image denoising via sparse 3D collaborative filtering with grouping constraint in luminance-chrominance space," in *2007 IEEE International Conference on Image Processing*, vol. 1, pp. I–313, IEEE, San Antonio, TX, USA, September 2007.

[47] M. Lebrun, M. Colom, and J. M. Morel, "The noise clinic: a blind image denoising algorithm," *Image Processing On Line*, vol. 5, pp. 1–54, 2015.

[48] J. Xu, L. Zhang, W. Zuo, D. Zhang, and X. Feng, "Patch group based nonlocal self-similarity prior learning for image denoising," in *Proceedings of the IEEE international conference on computer vision*, pp. 244–252, Santiago, Chile, December 2015.

[49] F. Wang, A. Eljarrat, J. Müller, T. R. Henninen, R. Erni, and C. T. Koch, "Multi-resolution convolutional neural networks for inverse problems," *Scientific Reports*, vol. 10, no. 1, pp. 1–11, 2020.

[50] B. Leung, G. Jeon, and E. Dubois, "Least-squares luma–chroma demultiplexing algorithm for Bayer demosaicking," *IEEE Transactions on Image Processing*, vol. 20, no. 7, pp. 1885–1894, 2011.

[51] J. Xu, L. Zhang, and D. Zhang, "External prior guided internal prior learning for real-world noisy image denoising," *IEEE Transactions on Image Processing*, vol. 27, no. 6, pp. 2996–3010, 2018.

[52] Neatlab, "Neat image," 2022, https://ni.neatvideo.com/home.

[53] S. Nam, Y. Hwang, Y. Matsushita, and S. J. Kim, "A holistic approach to cross-channel image noise modeling and its application to image denoising," in *Proceedings of the IEEE conference on computer vision and pattern recognition*, pp. 1683–1691, Las Vegas, NV, USA, June 2016.

[54] X. Jun, L. Hui, L. Zhetong, Z. David, and Z. Lei, "Real-world noisy image denoising: a new benchmark," 2018, https://arxiv.org/abs/1804.02603.